九州大学学術情報リポジトリ
Kyushu University Institutional Repository

Three-dimensional fatigue crack growth behavior in an aluminum alloy investigated with in-situ high-resolution synchrotron X-ray microtomography

Zhang, H.
Department of Production Systems Engineering, Toyohashi University of Technology

Toda, Hiroyuki
Department of Production Systems Engineering, Toyohashi University of Technology

Qu, P.C.
Department of Production Systems Engineering, Toyohashi University of Technology

Sakaguchi, Y.
Department of Production Systems Engineering, Toyohashi University of Technology

他

https://hdl.handle.net/2324/1807813

出版情報：Acta Materialia. 57 (11), pp.3287-3300, 2009-06-01. Elsevier
バージョン：
権利関係：

KYUSHU UNIVERSITY

Three-dimensional fatigue crack growth behavior in an aluminum alloy investigated with in-situ high-resolution synchrotron X-ray microtomography

H. Zhang, H. Toda, P.C. Qu, Y. Sakaguchi, M. Kobayashi

Department of Production Systems Engineering, Toyohashi University of Technology, 1-1, Hibarigaoka, Tempaku, Toyohashi, Aichi 441-8580, Japan.

K. Uesugi, Y. Suzuki

Japan Synchrotron Radiation Research Institute, 1-1-1, Kouto, Mikazuki-cho, Sayo-gun, Hyogo 679-5198, Japan.

Abstract

The fatigue crack propagation process in an Al-Mg-Si aluminum alloy was investigated using in situ high-resolution synchrotron radiation X-ray microtomography. Tomography datasets were obtained at periodic intervals throughout the 120000 fatigue cycles. 3D rendering of the through-thickness crack shape indicates that in a number of regions the adjacent sides of two branched cracks tend to overlap with fatigue cycling and form a crack overlapping region. Measured crack growth rates in each tomographic slice show that crack growth retardation generally occurs in these crack overlapping regions. The through-thickness variation in crack tip opening displacement was also measured and was used to account for the observed crack propagation behavior. Crack morphologies were observed at different load levels in a fatigue cycle. The crack closure level varied for two selected regions comprising different overlapping cracks. The correlation of the crack growth rate with both crack opening and closure levels was discussed and interpreted.

Keywords: Fatigue; Crack growth driving force; Crack closure; Crack tip opening displacement; Synchrotron radiation

1. Introduction

Three-dimensional (3D) fatigue crack propagation behavior inside a material has long been a concern for researchers because the interior crack growth rate differs from that at the surface. A

3D crack shape in the form of crack tunneling has even been observed in some thin-sheet aluminum alloy specimens [1,2]. Such through-thickness variation in crack propagation behavior is due to the change in the state-of-stress (or constraint) from plane stress at the surface to plane strain in the interior. An optical interferometry technique has been employed to determine the 3D crack tip position and to characterize crack closure loads along the crack front line in transparent polymer materials [3,4]. The results indicated the presence of crack tunneling and that the closure load at the specimen surface is higher than inside the material. Although crack opening behavior observed in polymers may reflect the corresponding behavior in metallic materials to some extent, there remains a need for quantitative information on such correspondence and a detailed study of the fracture behavior in metals.

To investigate the fatigue crack propagation rate behavior in the through-thickness direction in a metal or alloy, we must obtain information on the 3D crack front shape. In addition, crack closure is an important factor determining the crack growth rate. The stress state variation along a crack front line indicates that crack closure is a complex phenomenon. Some indirect methods for observing crack closure, such as a crack mouth clip gauge or a back face strain gauge, reflect the bulk crack opening load [5,6]. A near-tip strain gauge provides the local crack opening level for a certain distance behind the crack tip [7,8]. In these measurements, the crack closure load corresponds to the point at which the load-displacement curve deviates from linearity. While these compliance measurement methods are useful in the calculation of the effective stress intensity factor range by providing a single closure load, certain questions arise regarding the choice of a reasonable measurement position from which to obtain near-tip measurement results. Also, the direct correlation of such a single closure load with local crack growth behavior needs further investigation.

The crack closure behavior of an aluminum alloy was investigated by the direct observation of fatigue striations [9]. The crack opening load was determined by calculating the fatigue striation through the thickness in a special crack closure striation sequence. A higher crack

closure load has been observed at a specimen surface than in its interior. The use of this striation observation method is limited to through-thickness crack closure investigation. To determine the complex 3D morphology of cracks and secondary phases, another direct observation method is required. The serial sectioning technique has been utilized to visualize the 3D distribution of cracks and intermetallics [10,11]. Although the 3D distribution of microstructural features can be visualized, this method cannot be used to investigate microstructural variations at different load levels.

In recent years, X-ray microtomography has been employed to observe the 3D distribution of internal defects in bulk metal materials, such as micropores, grain boundaries and intermetallic particles [12-18]. An improved phase contrast technique and high resolution in the micrometer or even submicrometer range allow the use of X-ray microtomography to investigate crack morphology and crack closure behavior inside a material [19-24]. The use of the advanced third-generation synchrotron radiation facility SPring-8 in Japan for material science has made it possible to detect the 3D structure of defects with a resolution of better than 1 micrometer [22,25-27]. Deformation information has been obtained for the interior of a material by using a robust tracking method via a microtomography technique [26]. 3D strain distributions have been calculated by tracing the displacement of markers, thus providing an accurate tracking method for elucidating the relationship between a microstructure and local deformation and fracture [26]. Microtomography has been used to investigate the variation in the crack growth driving force along a crack front in an Al-Si-Mg aluminum alloy by measuring the local crack-tip opening displacement (CTOD) [25]. Local fracture toughness in such a dual phase material with a complex microstructure can be effectively characterized with this proposed CTOD technique. Local fracture resistance can be evaluated with this highly effective method.

The local fatigue crack growth rate depends on certain important factors, such as the local crack closure level and the stress intensity factor. With the high resolution of the tomography technique used in the present research, variations in the apparent crack tip along the crack front

line as functions of applied loads can be detected, making it possible to detect through-thickness crack closure behavior. In addition, near-tip crack opening measurements have proved to be more accurate than the driving force obtained with the particle displacement field based method [25]. Therefore, there is clearly a need to investigate these factors when determining the crack growth rates in real 3D cracks. This research aims to achieve in situ observation of the fatigue crack evolution process and to quantify the through-thickness crack tip opening behavior in an Al-Mg-Si alloy by using high resolution microtomography to investigate the factors influencing the crack growth rates. An aluminum alloy with a relatively low alloy element content was selected for this research. There are relatively few intermetallics particles distributed in the matrix and therefore the influence of the Al-Si eutectic phase observed in some aluminum alloys on crack face opening measurements can be avoided.

2. Experimental procedures

2.1 Material and specimen preparation

The material used in this work was a cast Al-Mg-Si alloy whose chemical composition is given in Table 1. To improve its mechanical properties and to break up its coarse casting microstructure, the as-cast alloy was hot rolled with multiple passes. Initially the as-cast ingot was divided into blocks that were 20 mm thick by 40 mm long and 20 mm wide. The block was subjected to multiple pass hot rolling with lubrication. Prior to each rolling the block was preheated to a temperature of 140 °C. A constant reduction of about 1 mm per pass was utilized. The final thickness of the sample was 4 mm. The rolled plate was heat-treated under the T6 condition with solution heat treatment at 530 °C for 5 hours followed by cold water quenching and artificial aging at 170 °C for 8 hours. A three-point bending (TPB) specimen was machined along an L-T orientation from the plate, and the specimen was 7 mm wide × 34 mm long × 4 mm thick. A notch with a radius of 0.1 mm was introduced by electro-discharge machining to allow easy precracking. Precracking was performed under load control. The load was reduced

during fatigue cycling when the ratio of the overall length including the notch and crack to the specimen width was around 0.5. The crack growth rate was controlled so that it was near the fatigue threshold of 1×10^{-10} m/cycle. After the precracking procedure, a small match-like parallelepiped specimen (12 mm long with a cross-section of 0.6 × 0.6 mm^2) containing a fatigue crack tip was carefully machined from the TPB specimen by electro-discharge machining, and aluminum tabs were glued to the two ends of the small specimen for the subsequent in situ loading of the specimen into the testing machine [25].

2.2 In-situ X-ray microtomography and fatigue testing

The microtomography experiment was carried out at beamline BL20XU at the synchrotron radiation facility SPring-8 in Hyogo, Japan. A highly coherent monochromatic X-ray beam with a photon energy of 20 KeV was obtained from a Si double crystal. A cooled 4000 × 2624 element charge coupled device (CCD) camera was used to capture the visible light, which was converted from the X-ray beam with a Ce-doped Lu_2SiO_5 scintillator. Based on the 2×2 binary modes used in the CCD camera the entire specimen cross-section and a height of 622 μm were captured by the CCD camera. The specimen to detector distance was set at 50 mm in the in-situ test to enhance the edge effect resulting from the phase contrast [28]. Typical experimental geometry for the tomographic imaging set-up and material test rig can be found elsewhere [25, 29].

The fatigue specimen was mounted on the test rig of a material test machine specially designed for in-situ X-ray tomography tests at SPring-8. The dedicated testing machine combined with a precision sample stage ensured accurate sample positioning during tomographic imaging. The fatigue loading of the small specimen was carried out under load control with a sinusoidal waveform, and a stress ratio R of 0.1. A test frequency of 20 Hz was selected. During fatigue cycling the maximum and minimum loads were 18 and 1.8 N, respectively. Once a crack extension was detected, the fatigue cycling was stopped at regular

intervals of 30000 cycles and a tomographic scan was performed. The fatigue test consisted of a total of 120000 cycles. After each interval the specimen was loaded to 18N by displacement control and maintained for 30 min before the tomographic scan to prevent any image blurring caused by stress relaxation. After fatigue cycling tomographic scans were also carried out for a number of selected load levels (18, 14.6, 11.4, 8.2, 5.0 and 1.8N) in order to observe the change in the crack tip at different load levels. A total of 1500 radiographs were obtained for each tomographic scan while the specimen was rotated 180 degrees along the specimen axis. This series of projections was reconstructed with a filtered backprojection algorithm to obtain the dataset of a 3D distribution map of the linear absorption coefficient. The isotropic voxels in the reconstructed image were $(0.474\ \mu m)^3$ in size.

2.3 Volume rendering and crack opening displacement measurement

The distribution of the linear absorption coefficient (LAC) in the reconstructed 16-bit dataset in the present aluminum alloy can be used to obtain information on the 3D distribution of cracks and microstructures. To reduce the data size a linear mapping program was employed to transfer the 16-bit LAC value (in the 0-60 cm^{-1} range) to an 8-bit grayscale image with a gray value range of 0 to 255. The key issue with respect to accurately extracting the whole crack volume is the choice of a reasonable gray value threshold in the 8-bit grayscale image to set the interface position between the crack and the matrix [25]. This threshold value was calculated to be 19.6, which corresponds to LAC value of 4.81 cm^{-1} in the 16-bit image. This is the intermediate value between the LAC peaks of air and aluminum. It should be noted that this intermediate value also corresponds to the valley between the air and aluminum peaks in the 16-bit LAC distribution.

To obtain quantitative information on crack opening, the crack volume was extracted in two steps: (1) a voxel on a 2D reconstructed slice was chosen, which was located in the crack and whose gray value was zero; (2) a 3D ‘seed’ growth technique was utilized to identify the volume of the crack. All voxels that are three-dimensionally connected to the chosen seed point in step

(1) and have a voxel gray value within the previously determined tolerance range are labeled as cracks. In this way, the boundary between a crack and the matrix has been set. Those voxels that belong to the crack are set at fully opaque, whereas the voxels belonging to the matrix are set at fully transparent. In this way, the 8-bit grayscale image was converted to a binary image containing gray values of either 0 (alloy) or 1 (crack). The crack tip opening displacement as a function of distance from the crack tip is calculated by counting the voxels in the crack volume between the two crack faces along the loading axis. In this measurement, the partial volume effect at the crack face must be taken into account [20]. This was calculated by using a gray value ramp between two neighboring voxels spanning the interface of two radiographically different phases. An error of half a voxel can be produced by this partial volume calculation. However, it has been found that such an error will not influence the reproducibility of the crack opening result as long as a reasonable threshold tolerance value is used [20].

3. Results and discussion

3.1 Through-thickness fatigue crack growth behavior

Fig. 1 shows a two-dimensional (2D) tomographic slice image of the reconstructed volume for a sample after 120000 cycles showing the fatigue crack and typical intermetallic particles. It corresponds to slice number 667 in Fig. 2(e). The image was obtained at a load level of 18N. Energy dispersive X-ray spectrometry revealed the light and dark color phases to be the AlFeSi and Mg_2Si phases (indicated by arrows), respectively. In terms of the density of particles AlFeSi and Mg_2Si, the average distances to the nearest-neighbor particle for the particle having a volume larger than 100 voxels in the 3D reconstructed volume, which were measured as the difference in the gravity center position, were calculated to be 13.6 and 17.06 μm for AlFeSi and Mg_2Si, respectively. To observe the change in the 3D crack shape in fatigue a three-dimensional representation of crack morphology was first obtained. As the gray levels of voxels corresponding to crack and porosity are generally lower than those of the Al matrix and

intermetallics particles, a straightforward method for extracting the crack from the tomographic dataset is to classify the crack and the matrix by setting a gray level threshold. However, cracks and pores with low gray levels will be extracted simultaneously, making it difficult to discern the crack tip location precisely. Therefore, the crack volume was obtained by using a 3D 'seed' growth technique and an appropriate threshold tolerance value as defined in the previous section. The extracted cracks were projected onto a plane perpendicular to the loading axis for different stages of fatigue, as shown in Fig. 2. Each slice corresponds to voxel edge length of 0.474 μm. All the crack images were obtained at the highest load of 18N in order to observe the entire crack front line. It is noted from the final fatigue stage that the crack propagation is retarded by fatigue cycling in a number of regions, such as those labeled A, B and C in Fig. 2(e). Such retardation, especially that in regions B and C, can also be observed in the previous fatigue stages (a)-(d). This persistent growth retardation in roughly the same region during fatigue cycling will be discussed in detail below. Observation of the crack front profile revealed several features of crack propagation. Localized crack growth is frequently observed. Sometimes, a general crack front line can be observed behind the localized crack growth, as found (see arrows) on the two sides of region B in the 30000-cycle sample. In the final stage of fatigue a general line can be seen more clearly in the dotted rectangle region in Fig. 2(e). It appears that the sensitivity of a crack to microstructural inhomogeneity gradually decreases in this region during this fatigue stage. 3D crack tip position at different stages of fatigue can also be observed by plotting crack tip coordinate along specimen thickness for each fatigue stage (Fig. 3), from which the process of fatigue crack propagation can be studied.

To provide quantitative information on crack growth, the calculated crack growth rates are shown in Fig. 4 (a) to (e) by taking the crack extension at each 30000 cycle interval and for the entire 120000 cycles in order to compare crack growth at different stages. Dashed lines indicate the average crack growth rates for each 30000 cycle interval. Crack growth along the thickness direction appears to be inhomogeneous. In the initial three intervals, crack propagation is

relatively slow, and the average growth rates along the thickness are 4.67×10^{-10}, 4.44×10^{-10} and 4.67×10^{-10} m/cycle, respectively, which is near the threshold region of fatigue crack growth. In the final 30000 cycles, the average crack growth rate increased to 1.43×10^{-9} m/cycle. From observation of the total 120000 cycles, crack growth retardation generally falls into three regions, i.e., between slice numbers 100 and 200, 750 and 800, and 1000 and 1100. These regions are also consistent with the crack growth retardation seen in Fig. 2.

3.2 3D observation of crack overlapping and crack morphology development

Fig. 5 shows a 3D rendering of a crack in the 120000-cycle sample highlighting the crack geometry and the crack front profile. The image was obtained at the maximum load. The main crack can be seen to separate into several segments in a number of regions, such as A, B and C, as shown in Fig. 5(b)-(d). In addition to the front light source, a side light source positioned 45° to the right of the observer was also used to highlight these crack segments. Observations of regions B and C indicate that the two segments propagated along both the depth (Y axis in Fig. 5(a)) and width (X axis in Fig. 5(a)) directions after their separation from the main crack. While this 3D representation of the crack provides qualitative information on these crack segments, observation of a 2D tomographic slice image can reveal the development of these cracks and their interaction with fatigue cycling quantitatively. Fig. 6 shows a series of slices of the 120000-cycle sample cut from the 3D rendered image. These slices are perpendicular to the crack growth direction at different distances from the crack tip. Fig. 6(a) to (c), respectively, highlight the observation of two crack segments at positions 337, 222 and 93 pixels from the crack tip in the region labeled A in Fig. 2. Fig. 6(d) to (f), respectively, show the development of another pair of segments in region B in Fig. 2 with the slice positioned 380, 336 and 249 pixels from the crack tip. Before separation from the main crack the two segments were seen to be connected to each other in a segment of a twisted crack. In Fig. 6(a) the two cracks are connected by a short segment nearly parallel to the loading axis. As regards the crack in region

B, two cracks were located at the same twisted crack before separation, as shown in Fig. 6(d). In both regions A and B these segments propagated along either the depth or width direction, and can be seen to overlap each other at the adjacent crack front when they are viewed along the loading direction. For the pair of segments in region B, the two cracks were seen to deviate from their original twisted crack orientation and gradually propagate along a plane perpendicular to the loading axis with fatigue cycling.

To better understand the evolution of crack geometry during fatigue cycling with respect to the pairs of overlapping cracks, part of the overlapping segments of the 0 (before fatigue), 60000 and 120000-cycle samples were extracted from the tomographic data, and projections of the segments on a plane perpendicular to the loading axis were observed, as shown in Fig. 7. The segments for the three fatigue stages (0, 60000 and 120000 cycles) were extracted at positions 278 and 388 pixels from the crack tip of the 120000-cycle sample along the depth direction (Y axis in Fig. 7) for the regions labeled A and B in Fig. 5, respectively. Only segments from the 120000-cycle sample are shown. The crack front profile of the 0 and 60000-cycle samples are shown as solid lines. Fig. 7(a) and (b) show the two overlapping segments (labeled A1 and A2) in region A in Fig. 5. Crack A1 corresponds to the left-hand part of region A in Fig. 2(e), whereas A2 corresponds to the right-hand part of region A (see arrows). For comparison, the overlapping segments in region B of Fig. 5 are shown in Fig. 7(c) and (d) as B1 and B2 indicating the left and right-hand parts of B in Fig. 2(e) (see arrows), respectively. To provide the extension of the overlapping segment in the depth and width directions during fatigue cycling quantitatively, the two pairs of segments from the three samples (0, 60000 and 120000 cycles) are positioned in Fig. 7 based on their respective positions in the coordinate system. On the basis of the 3D crack tip position at three fatigue stages (0, 60000 and 120000 cycles), crack extension in both the depth and width direction were quantified. First, reference points for crack extension measurement for the two pairs of overlapping segments in region A and B were defined. In the depth direction, the reference points are located on planes which are

278 and 388 pixels from the crack tip of the 120000-cycle sample (bottom line of Fig. 7(a)-(d)) for regions A and B, respectively. In the width direction, the reference points are defined to be the midpoint between the two outermost points of the crack front line of the pair of overlapping segment in the width direction for the 0-cycle sample, as shown in Fig. 7.

To measure crack extension, measurement point in the depth direction was defined as the intersection point of the projected crack front line with the auxiliary plane (dotted straight lines, parallel to the loading axis) extending from the reference point. The measurement point in the width direction was the outermost point of crack front line in the width direction. In this way, the magnitude of crack extension in the depth direction (L_{DA1} and L_{DA2} for region A, and L_{DB1} and L_{DB2} for region B) was the distance from the reference point to the measurement point (intersection point) in the depth direction. Crack extension in the width direction (L_{WA1} and L_{WA2} for region A, and L_{WB1} and L_{WB2} for region B) was the distance from the reference point to the measurement point (outermost point) in the width direction, as shown in Fig. 7.

In Fig. 8, the development of the crack geometry in terms of the crack extension in the depth and width directions after 60000 and 120000 cycles is compared for the two regions labeled A and B in Fig. 5. The figure also shows the offset distances, i.e., the distances between the two overlapping segments along the loading axis, which were measured as the distances between the intersection point of the crack front line with the auxiliary plane along the loading axis in Fig. 7. From Fig. 8(a), it is noted that there is no significant difference in the magnitude of the crack extension in the width direction between the two overlapping segments in region A over 120000 cycles. A measurement along the depth direction for region A also reveals a similar trend. However, in region B of Fig. 5, the crack growth rates in both the depth and width directions were clearly faster for crack B1 than for crack B2. The change in the crack geometry in fatigue can also be observed from their offset distance in the loading direction. The offset distance between the two cracks in the loading direction in region A increased from 27.9 to 31.8 μm during the 120000 cycles, whereas the offset distance for the cracks in Fig. 7(c) and (d)

increased from 25.1 to 44.1 μm.

From the above observations on changes in the crack geometry of the two pairs of overlapping segments in regions A and B, it appears that the difference in the degree of crack growth retardation between regions A and B is due to different interactions between the overlapping segments. Previous researches on the interaction between two parallel surface cracks have indicated that when the two cracks are close to each other or when the offset between the two cracks decreases the interaction between cracks may affect the stress field as well as the crack growth rate [30-32]. These researches also revealed that stress intensity factors decrease when there is sufficient overlapping between the two cracks [31,33]. This reduction in the crack driving force was believed to be due to stress shielding caused by the parallel cracks. Although the crack geometry and pattern in the present study differ from those of parallel cracks, they may share similar stress shielding mechanisms. Research on interacting parallel cracks has indicated that stress shielding becomes strong when the offset between the two cracks decreases [31,33]. Therefore, it appears that the relatively larger crack growth retardation observed in region A is due to the stronger stress shielding effect of the overlapping segments in that region where the offset distance between the segments is smaller. In this case, the stress at the crack tip is reduced, leading to retardation of crack propagation.

In Fig. 7, the macroscopic shapes of the crack were found to be smooth although there are frequently local undulations or sharp protrusions. Therefore a gradual variation in the stress intensity factor (SIF) along the crack front is assumed in the overlapping crack segment. The SIF decreases along the crack front and falls to a relatively low level at the overlapping segments, finally reaching a very low value in regions where the two overlapping segments gradually converge. From these analyses we can deduce that the entire crack around an overlapping region will experience a stress shielding effect, and this effect is pronounced in the overlapping portion. Therefore the existence of crack overlapping leads to a reduction in crack growth rates. This shielding effect is mitigated when the offset distance between the overlapping

cracks increases with fatigue cycling. Another feature of the observation of the two pairs of overlapping segments is that, in contrast to the relatively uniform extension of cracks A1 and A2 in both the depth and width directions (Fig. 7(a) and (b)), the extension of crack B1 along the depth and width directions occurs more easily than with crack B2, as noted from Fig. 7(c) and (d). The extension in width of B2 is even smaller than that of cracks A1 and A2 although the offset distance between B1 and B2 is larger than that for A1 and A2. In research on the interaction between parallel cracks, Kamaya has indicated that relative crack size has a significant influence on the propagation behavior of the two cracks [32]. The observation of region B in Fig. 2 indicates that the length of crack B2 is always smaller than that of crack B1 during the fatigue cycling. After separation from the twisted crack, the extension of the width of crack B2 is strongly affected by the presence of B1. As the length of crack B1 is larger than that of crack B2, an extension of B2 towards B1 will cause a higher degree of overlapping. By contrast, B1 can extend easily owing to the insignificant crack shielding from crack B2. Therefore, the extension behavior of the pair of overlapping cracks is a competitive process that depends on their initial crack front positions.

The mechanism by which a crack overlap is formed from a main crack is still not completely clear in the present material. One supposition is that a flat crack may be deflected in two different directions when it encounters two grains with different crystallographic orientations. The grain boundary wetting technique employed in tomography or EBSD surface mapping methods can be used to reveal the grain boundary structure, by which the interaction between a fatigue crack and a grain boundary can be studied. Beside grain boundary, crystallographic crack growth may also contribute to crack deflection in near-threshold regime of fatigue crack propagation in a material. Hanlon et al, has indicated that periodic crack deflection may be one of the reasons for the increase in threshold SIF in a coarse grain structure [34]. In the present material, crack deflections have been observed along crack path, as shown in Fig. 10(b). Therefore, the crystallographic information in the present material is also important to

understand the formation mechanism of crack overlapping. It is noted from Fig. 6(d) to (f) that the two overlapping cracks gradually converge to a twisted crack as the distance behind the crack tip increases. The propagation of a crack sometimes twists away from its nominal mode I growth direction due to its interaction with a microstructural inhomogeneity, such as a grain boundary. The propagation of the twisted crack appears slow compared with a neighboring horizontal planar crack due to a reduction in the effective driving force. This portion of twisted crack becomes sensitive to microstructure due to its low crack growth rate, and will tend to separate into two segments when it encounters internal defects, such as intermetallics particles, pores or grain boundaries. The subsequent propagation of the segment tends to deviate from its initial twisted plane and gradually adjusts itself to a horizontal and planar path, i.e., along the path of maximum driving force [35]. It was noted in the previous section that a pair of overlapping crack segments with a smaller offset distance may have more pronounced shielding effect. This implies that a small twisted crack is helpful for the promotion of crack growth retardation when two overlapping segments are initiated. On the other hand, before the initiation of overlapping, a large twisted crack is beneficial as it tends to induce higher crack shielding. This dilemma is related to certain factors deciding the formation of overlapping crack segments, such as crack growth rate, grain size, and defect distribution. Therefore, further research on the formation conditions and mechanisms of crack overlapping is needed for material microstructure designation in order to improve fatigue performance.

3.3 Crack growth driving force

The crack tip opening displacement (CTOD) method is a well established technique for calculating the crack growth driving force. This method is more useful for observing crack opening contours along a crack front line when the 3D crack volume is obtained by microtomography. Fig. 9(b) shows the variation in the crack tip opening displacement range (ΔCTOD) in each tomographic slice along the specimen thickness for the 120000-cycle sample

in a 1.8 to 18N load range. The measurement points were 10 pixels (4.74 μm) from the crack tip for each slice. Also shown in the figure is the through-thickness position of crack tip (Fig. 9(a)), from which three large crack overlapping regions around slice numbers 145, 775 and 1030 (corresponding to regions A, B and C in Fig. 5) and a small crack overlapping region around slice number 317 can be found. When the difference in crack length was smaller than 10 pixels for two overlapping cracks the maximum value of ΔCTOD was selected. The larger crack opening in region D in Fig. 9(b) correlated with a single and relatively planar crack with a macroscopic smooth crack front, similar to that in the dotted rectangle in Fig. 2(e). A typical crack opening contour in this region can be observed in the tomographic slice in Fig. 10(a), which corresponds to slice number 527 specified in Fig. 2(e). A large crack opening can also be found near the specimen surface, such as region F in Fig. 9(b), where there is also a single crack near the crack tip. Typical crack contour in one of the slices in this region can be seen in Fig. 10(c), which corresponds to slice number 1197 specified in Fig. 2(e). The cracks tend to deflect from their Mode I propagation plane in the two surface regions, and this deflection becomes more prominent near specimen surface. In contrast to the large crack opening observed in regions D and F, the crack morphology of the relative small crack opening in region E in Fig. 9(b) is shown in Fig. 10(b), which shows two overlapping cracks. The difference between their crack lengths is 23 μm, and the measured ΔCTOD from the upper crack is 1.87 μm. It is also noted that the magnitudes of the crack openings are relatively small between region D and F in Fig. 9(b) although crack overlapping does not exist throughout this region. The single crack portion between regions D and E in Fig. 9(b), which extends from slice number 816 to 991, is located between two overlapping regions. Owing to the small crack opening in the neighboring overlapping regions, the opening of crack in this single crack portion will be restricted. Based on the above observations, the CTOD is relatively small in the three overlapping regions, whereas it is large outside these regions. Also, there are more crack contact points (zero crack opening) in the overlapping region, further indicating a small opening in this region. From the

observed crack growth rate plots shown in Fig. 4, small crack opening is correlated with slower crack growth. This is consistent with the observation that the fatigue crack growth rate is directly related to the range of the crack-tip opening displacement [36].

Owing to the microstructural inhomogeneity in the aluminum alloy, which makes the crack face opening irregular in localized regions, the physical displacement of intermetallic particles in a fatigue cycle has been utilized to calculate the crack growth driving force along the front line of a 3D crack [19]. This was undertaken by tracking the centroid position of the intermetallic particles or micropores in a specimen to obtain 3D displacement of each particle or micropores. The crack growth driving force along the crack front line can be calculated based on the obtained 3D distribution of the displacement field around the crack tip. Recently, a more accurate tracing method has been developed by incorporating a newly developed macroscopic trajectory prediction technique and a modified spring model algorithm method [26]. By using this particle tracing method, the AlFeSi intermetallic particles in the elastic K-dominated zone around a fatigue crack tip were selected as tracking markers to calculate the mixed-mode displacement for two sets of positions corresponding to the maximum and minimum load levels of 18 and 1.8N, respectively. The calculated Mode I stress intensity factor range as a function of crack front position is shown in Fig. 9(c). Three relatively large peaks of driving force value were noted (indicated by arrows). However, when we look at the crack growth rate data in Fig. 4, we cannot find a good correlation between these peak driving force values and the fast crack propagation in either the entire 120000 cycles or in a certain periodic interval, such as the last 30000 cycles. By contrast, the three peaks are located at crack growth retardation regions A, B and C in Fig. 2.

From the relationship between crack driving force and 3D displacement field, the factors deciding the driving force are the polar coordinate of a particle relative to the crack tip and the Mode I and II displacements of that particle [19]. Observation of the calculated displacement field of the particles shows that Mode I displacements are larger along these three overlapping

regions. This means that local compliance is increased by the existence of the overlapping crack. This suggests that a high crack growth driving force is associated with increased compliance in the crack overlapping region. Therefore, the issue of crack interaction must be addressed when using the displacement field based local driving force method. When using this approach, the deformation behavior at a local crack tip is the average for each particle in a slice containing that crack tip. Damage in neighboring slices or bulk deformation away from near-tip region will also influence the final result. By contrast, local fatigue crack growth resistance along a crack front can be evaluated by using the direct crack tip opening displacement measurement method, especially in the present study where Mode I crack propagation is dominant in the later stage of fatigue. Also, as discussed below, the use of the crack tip opening displacement method enables us to compare near-tip crack closure behavior along a crack front, and to reveal the magnitude of the constraint on crack opening imposed by adjacent overlapping cracks qualitatively. It should be noted that the particle displacement method could provide relatively accurate information on the variation in the local compliance inside a material when there is a complex crack interaction. Also, the crack face displacement derived from a pair of particles spanning the crack face can be used to verify the result obtained from direct measurement as long as the deformation in the material between the particles and the crack face is taken into account.

3.4 Crack face contact at different load levels

The through-thickness crack profile of the 120000-cycle sample was observed at a number of selected load levels to determine the degree of crack closure by following the variation in the apparent crack tip position. The first dataset was collected at the maximum load of 18N, and the other datasets were obtained with decreasing loads of 14.6, 11.4 8.2, 5.0 and 1.8N. Fig. 11 shows projections of a crack front profile onto a plane perpendicular to the loading axis. The crack in Fig. 11(f) is the same as that in Fig. 2(e), which shows the crack of the 120000-cycle sample obtained at the maximum load. The local crack growth directions are different because

of local undulation or sharp protrusion in the crack contour. A number of cracks can be seen to extend in the lateral direction, as shown on the rightmost portion of Fig. 11(f). To observe the change in the apparent crack along the depth direction clearly, two regions were selected, which correspond to slice number in the range 500 to 750 and 930 to 1050, respectively, as indicated by regions G and H in Fig. 11(f). These two regions are from different portion of the entire crack front line, i.e., the portion between A and B and between B and C in Fig. 5. Another feature of the two regions is that both contain a single crack and a portion of the crack near the crack overlapping region. In Fig. 11(f), the overlapping crack portion is in the right hand part of regions G and H. It is also noted that the magnitude of the crack tip opening in these two regions is different, with the relatively larger opening observed in region G (Fig. 9(b)).

Observation of the crack front contour reveals some interesting features. The crack images G and H in Fig. 11 show that the crack front line at 18N conforms macroscopically to a general line without many sharp protrusions, although a local undulation can be observed from a microscopic point of view. This general contour remains at 14.6N. The above case cannot be observed clearly at 11.4N because the local crack tip has closed. At a lower load level, a baseline along a general line can be seen in region G at 5.0N where a number of cracks protrude sharply from the line. At 1.8N, a general line can be seen more clearly in both regions G and H, and fewer crack protrusions remain above the line in region G. The remaining crack protrusions in this region at a low load indicate that the magnitude of the plastic part of the CTOD range $\Delta CTOD_{pl}$ is different along crack fronts in this region, and there is large crack-tip damage in region G. On the other hand, few crack protrusions can be observed in region H even at 5.0N, indicating premature crack tip closure in this region.

To provide quantitative information on crack tip closure during unloading changes in apparent crack length as a function of load in regions G and H was quantified, as shown in Fig. 12. Firstly, the difference in apparent crack length between the maximum and the minimum load was calculated, as shown in Fig. 12(a) and (c). The changes in apparent crack length with

decreasing load (called closure length) were also examined in the two regions in order to follow the position of the near-tip residual crack opening as a function of load, as shown in Fig. 12(b) and (d). The average closure lengths from 18 to 1.8N in the two regions are 45.6 and 52.7 pixels, respectively. As seen in Fig. 12(a) and (c), for about 60% of the all slices the closure length is in the 40 to 60 pixel range. This relatively insignificant variations in closure length along most of the crack front in these regions are assumed to be due to the observation that there are relatively few large asperities, i.e., the apparent sliding and contact of the crack faces will mitigate in the later stages of fatigue cycling. The minimum closure length is at slice numbers 607 and 655, which are located in region G. Such small crack closure length is consistent with the relatively large residual crack opening in region G in Fig. 11. In Fig. 12(b) and (d), the changes in apparent crack tip position at a number of selected and decreasing loads of 18, 14.6, 11.4 8.2, 5.0 and 1.8N are compared as functions of the tomographic slice position. The maximum spacing between crack position measured along the vertical direction in these curves corresponds to the closure length in Fig. 12(a) and (c). When the load is reduced from its maximum value to 14.6N nearly the entire crack front remains unchanged except for a small zone in the right hand part of region H. Similarly, in the final unloading stage, i.e., from 5.0 to 1.8N, the change in the apparent crack tip is confined to a small zone between slice numbers 607 and 643. Large crack-tip residual plastic opening has been observed in this zone. The above observations indicate that most of the crack closures occurred in load range of 14.6 to 5.0N for the two regions. When the load decreases further from 14.6 to 11.4N, most of the part in region G remains unchanged, whereas more than half of the crack tip region begins to retreat in region H. In the 11.4 to 8.2N range, the cracks in the right half in region G still remain unchanged, but all the cracks in region H continue to close except for a short segment with a length of 15 pixels around slice 1010. From 8.2 to 5.0N, crack face contact can be found at the two sides of region G. However, the crack closure activities reduce significantly in region H.

The observation of the changes in the apparent crack tip position at different load levels

indicates that profuse crack face contact occurs in the 11.4 to 5.0N load range in region G and from 14.6 to 8.2N in region H. It is also noted that at the same unloading interval in load range of 14.6 to 5.0N more of the crack tends to close in region H than in region G. All these results indicate that the crack closure level in region H is greater than that in region G. This different closure level appears to be due to fact that G and H are located in different crack portions in the 3D crack volume. Region G is near an overlapping crack segment in region B seen in Fig. 5, whereas region H is located between overlapping region B and C in Fig. 5. Crack opening in regions G and H was constrained by the two overlapping cracks B1 and B2 in region B, respectively. However, the constraint on crack opening imposed by crack B2 is more significant than that imposed by crack B1. [1] In addition, the crack opening in region H was also constrained by the overlapping crack in region C shown in Fig. 5. Owing to the difference in the constraints imposed by the overlapping regions, the crack opening is smaller in region H than in region G, as substantiated from CTOD measurement results in Fig. 8(b). Therefore, the higher crack closure level observed in region H is assumed to be due to the smaller crack opening level in this region.

The 3D crack volume and the development of crack geometry in the present material can be visualized by using microtomography. During crack propagation, two crack segments tend to separate from the main crack and propagate independently. A small overlapping region forms at the adjacent side of the two segments. When the traditional 2D surface observation method is used an overlapping region intersecting the specimen surface has the appearance of crack branching. However, from observations of the present material, a fully forked crack cannot form. Therefore, an investigation of crack morphology and its development solely based on surface observations will provide an irrelevant result.

From the near-tip opening results in Fig. 9 as well as from the observed through-thickness

[1] Note that in region B propagation along both the depth and width directions is much easier for the overlapping crack near region G than for the overlapping crack near region H.

variation in the crack growth rate, it can be seen that CTOD range is directly correlated with the crack growth rate. This indicates that CTOD is a useful tool for characterizing the crack growth driving force and can be used directly for correlation with crack growth rates. It is noted that the CTOD is relatively small in the overlapping region. Such a small crack front opening also leads to premature crack closure (see Fig. 12). This enhanced crack closure level will further reduce the crack growth rates. The investigation of interaction of two offset parallel cracks has shown that Mode III displacements are relatively large at an overlapping crack front compared with other crack front regions [30]. Based on these calculations, the Mode III displacement produced at the overlapping region in the present material will further reduce the crack growth rates.

Conclusion

The X-ray microtomography technique has proved to be a useful tool for performing the in situ visualization of 3D fatigue crack propagation in the interior of an Al-Mg-Si alloy. 3D fatigue crack geometries and their development have been quantified as functions of applied loads, and this cannot be realized by traditional surface observation methods. Local variations in crack tip openings has been found to be relevant to the crack growth rate and to crack closure behavior, which indicates the feasibility of using this parameter in the micromechanical analysis of fatigue cracks in small tomography specimens. After investigations of the 3D crack evolution process and the crack tip opening contour, the following conclusions were obtained:

1) As found with conventional fatigue experiments, the through-thickness crack growth rates in the present specimen increased with fatigue cycling. Crack propagation retardation always occurred at a number of regions where the main crack separates into two segments. The overlapping part of two crack segments induces a shielding effect as regards crack propagation along both the depth and width directions.

2) The crack overlap formation mechanism may be different for different regions in the present material. However, observations of one of them have indicated that two crack segments were

initiated by a twisted crack, deviated from their original twisted crack orientation and gradually propagated along a plane perpendicular to the loading axis with fatigue cycling.

3) The extension of a pair of overlapping crack segments is a competitive process, depending on the initial crack front positions. The longer segment propagates faster along either the depth or width direction, whereas extension of the shorter one was constrained, especially along the width direction.

4) The measured through-thickness variation in crack tip opening displacement shows that the crack opening is relatively smaller around an overlapping region than that for a single planar crack. This can explain the observed low crack growth rates around crack overlapping regions. The relatively small crack tip opening in the crack between regions B and C in Fig. 5 appears to be due to strong constraint from the adjacent overlapping crack. Based on the particle displacement field based method the high crack growth driving force is associated with increased compliance in the crack overlapping region.

5) Different crack closure levels were observed for two crack portions located at different positions relative to the overlapping region. The portion of crack with the lower crack opening induces the higher closure stress.

Acknowledgements

The synchrotron radiation experiments were performed at the SPring-8 with the approval of JASRI (Proposal No. 2006B1018). This work was supported by Grant-in-Aid for Scientific Research (Nos. 17360340 and 18-06407) from the Japan Society for the Promotion of Science (JSPS). This work was also supported in part by the Light Metal Educational Foundation. H.Z. gratefully acknowledges the support of Japanese Society for the Promotion of Science (JSPS) through a JSPS Fellowship Program.

References

[1] Newman Jr. JC, James MA, Zerbst U. Eng Fract Mech 2003;70:371.

[2] Heerens J, Schödel M. Eng Fract Mech 2003;70:417.

[3] Ray SK, Grandt Jr. AF, Andrew S. Three-dimensional measurement of fatigue crack closure and opening. In: Wei RP, Gangloff RP, editor. Basic questions in fatigue. Vol. II ASTM STP 924, 1980. p.275.

[4] Ray SK, Grandt Jr. AF. Comparison of methods for measuring fatigue crack closure in a thick specimen. In: Newman Jr. JC, Elber W, editor. Mechanics of fatigue crack closure. ASTM STP 982; 1988. p.197.

[5] Xu YG, Gregson PJ, Sinclair I. Mater Sci Eng 2000;A284:114.

[6] Donald K, Paris PC. Int J Fatigue 1999;21:S47.

[7] Macha DE, Corbly DM, Jones JW. Exp Mech 1979;19:207.

[8] Carboni M. Eng Fract Mech 2007;74:563.

[9] Dawicke DS, Grandt Jr. AF, Newman Jr. JC. Eng Fract Mech 1990;36:111.

[10] Dudek MA, Chawla N. Mater Charact 2008;59:1364.

[11] Sidhu RS, Chawla N. Scripta Mater 2006;54:1627.

[12] Stock SR. Int Mater Rev 1999;44:141.

[13] Ludwig W, Buffière J-Y, Savelli S, Cloetens P. Acta Mater 2003;51:585.

[14] Maire E, Bouaziz O, Di Michiel M, Verdu C. Acta Mater 2008;56:4954.

[15] Ohgaki T, Toda H, Sinclair I, Buffière J-Y, Ludwig W, Kobayashi T, Niinomi M, Akahori T. Mater Sci Eng 2005;A406:261.

[16] Baruchel J, Buffière J-Y, Cloetens P, Di Michiel M, Ferrie E, Ludwig W, Maire E, Salvo L. Scripta Mater 2006;55:41.

[17] Ignatiev KI, Davis GR, Elliott JC, Stock SR. Mater Sci Tech 2006;22:1025.

[18] Toda H, Uesugi K, Takeuchi A, Minami K, Kobayashi M, Kobayashi T. Appl Phys Lett 2006;89:143112.

[19] Toda H, Sinclair I, Buffière J-Y, Maire E, Khor KH, Gregson P, et al. Acta Mater 2004;52:1305.

[20] Toda H, Sinclair I, Buffière JY, Maire E, Connolley T, Joyce M, et al. Phil Mag A 2003;83:2429.

[21] Guvenilir A, Breunig TM, Kinney JH, Stock SR. Acta Mater 1997;45:1977.

[22] Qian L, Toda H, Uesugi K, Kobayashi M, Kobayashi T. Phys Rev Lett 2008;100:115505.

[23] Khor KH, Buffière J-Y, Ludwig W, Sinclair I. Scripta Mater 2006;55:47.

[24] Maire E, Carmona V, Courbon J, Ludwig W. Acta Mater 2007;55:6806.

[25] Toda H, Yamamoto S, Kobayashi M, Uesugi K, Zhang H. Acta Mater 2008;56:6027.

[26] Kobayashi M, Toda H, Kawai Y, Ohgaki T, Uesugi K, Wilkinson DS, Kobayashi T, Aoki Y, Nakazawa M. Acta Mater 2008;56:2167.

[27] Qian L, Toda H, Uesugi K, Kobayashi T, Ohgaki T, Kobayashi M. Appl Phys Lett 2005;87:241907.

[28] Cloetens P, Pateyron-Salomè M, Buffière J-Y, Peix G, Baruchel J, Peyrin F, Schlenker M. J Appl Phys 1997;81:5878.

[29] Toda H, Ohgaki T, Uesugi K, Kobayashi M, Kuroda N, Kobayashi T, Niinomi M, Akahori T, Makii K, Aruga Y. Metall Mater Trans A 2006;37A:1211.

[30] Cisilino AP, Aliabadi MH. Int J Pres Ves Piping 1997;70:135.

[31] Kamaya M. Eng Fract Mech 2008;75:1350.

[32] Kamaya M. Japan Soc Mech Engineers 2003;46:15.

[33] Tsang DKL, Oyadiji SO, Leung AYT. Eng Fract Mech 2003;70:2199.

[34] Hanlon T, Kwon Y.-N, Suresh S. Scripta Mater 2003;49:675.

[35] Anderson TL. Fracture mechanics. Third ed. Boca Raton, FL: CRC Press, 2005. p.81.

[36] Höppel HW, Kautz M, Xu C, Murashkin M, Langdon TG, Valiev RZ, Mughrabi H. Int J Fatigue 2006;28:1001.

Figure captions

Fig. 1 Reconstructed slice image showing typical fatigue crack and microstructural constituents in the present Al-Mg-Si alloy.

Fig. 2 Projection of part of fatigue crack volume on a plane (X-Y) perpendicular to the loading axis. The crack front profiles at different stages of fatigue cycling from 0 cycle (a) to 120000 cycles (e) are highlighted.

Fig. 3 Through-thickness positions of crack tip for different stages of fatigue cycling from 0 cycle (a) to 120000 cycles (e).

Fig. 4 Fatigue crack growth rates measured at different fatigue intervals. The growth rates were calculated for every 30000 cycles ((a) to (d)) and for the total 120000 cycles (e). Dashed lines indicate the average crack growth rates for each 30000 cycle interval.

Fig. 5 3D rendering of the crack volume extracted from the 120000-cycle sample. The image was obtained at the maximum load. Typical crack overlapping regions are labeled A, B and C. A side light source was positioned 45° to the right of the observer to highlight the crack in these regions. (b)-(d) are magnified views of crack overlapping regions A, B and C in (a), respectively.

Fig. 6 Reconstructed slice images of the 120000-cycle sample showing crack morphology at different distances from crack tip: (a)-(c) indicate the development of two overlapping crack segments in region A in Figure 5; (d)-(f) indicate another pair of overlapping segments in region B in Figure 5. The slices are perpendicular to the crack growth direction. Arrows indicate the

pair of overlapping crack segments.

Fig. 7 Evolution of a pair of overlapping crack segments with fatigue cycling: (a)-(b) indicate two overlapping segments A1 and A2 (as marked in Fig. 6(c)) in region A in Fig. 5; (c)-(d) indicate another two overlapping segments B1 and B2 (as marked in Fig. 6(f)) in region B in Fig. 5. Loci of projected crack front at 0 and 60000 cycles were also shown. The measurements of crack extension in the depth and width direction, L_{DA1}, L_{DA2}, L_{WA1}, L_{WA2}, L_{DB1}, L_{DB2}, L_{WB1}, L_{WB2}, are described in more detain in the text.

Fig. 8 Variation of crack geometries of two pairs of overlapping crack segments with fatigue cycling. Crack extensions in the depth (L_{DA1}, L_{DA2}, L_{DB1} and L_{DB2}) and width direction (L_{WA1}, L_{WA2}, L_{WB1} and L_{WB2}) were calculated at three stages of 0, 60000 and 120000 cycles for regions A and B in Figure 5 (solid symbol, left axis). The changes in offset distance along loading direction between the two pairs of segments were also calculated (open symbol, right axis).

Fig. 9 Variation in the crack driving force in each tomographic slice along the specimen thickness for the 120000-cycle sample: (a) through-thickness position of crack tip; (b) variation in the crack tip opening displacement range in a 1.8 to 18N load range; (c) Mode I stress intensity factor range as a function of crack front position. The three arrows in (c) indicate the positions of peak driving force.

Fig. 10 Tomographic slice images showing typical crack tip morphology of (a) a straight and planar crack in region D in Fig. 9(b), (b) overlapping crack segments in region E and (c) a gradually deflected crack observed in region F near specimen surface.

Fig. 11 Crack volume viewed along loading axis for the 120000-cycle sample. In (a) to (f) the

cracks were observed at different load level from 1.8 to 18N. Two crack regions G and H in (f) were selected to highlight the variation in the crack tip positions with load.

Fig. 12 Comparison of apparent crack tip positions during unloading in two regions G and H in Fig. 11(f). The difference in apparent crack length between the maximum and the minimum load in the two regions is shown in (a) and (c). In (b) and (d) the changes in apparent crack tip position at a number of selected loads are compared as functions of the tomographic slice position.

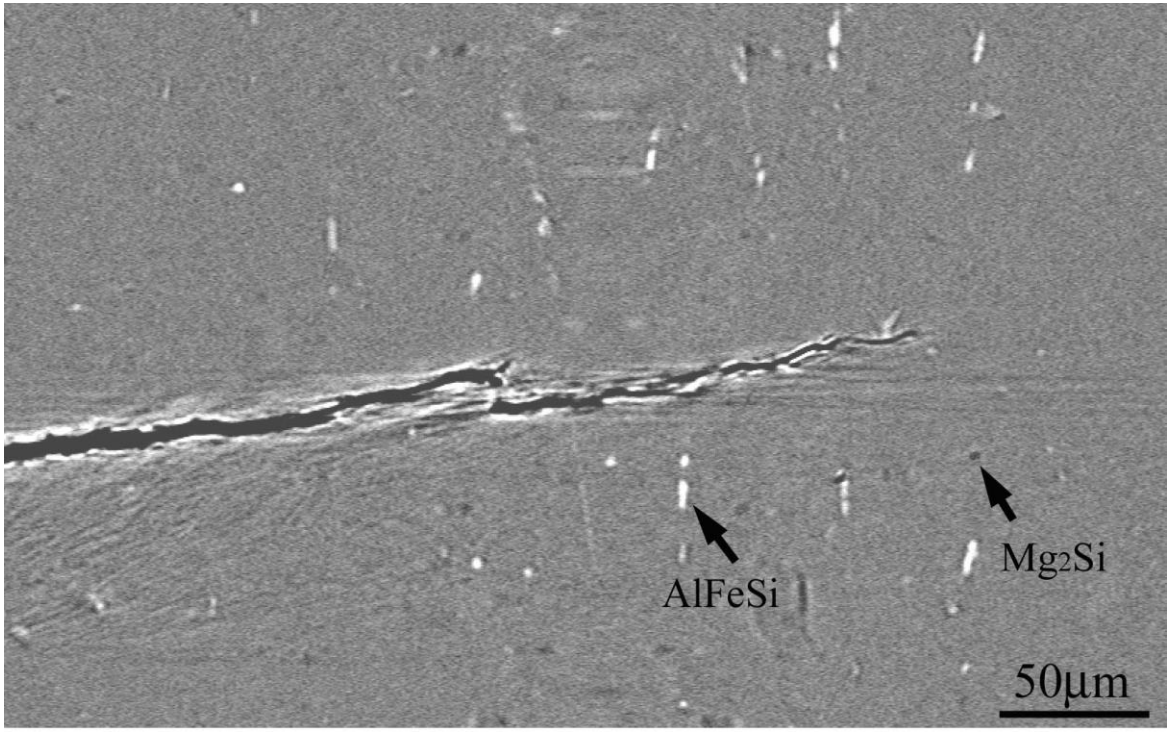

Figure 1

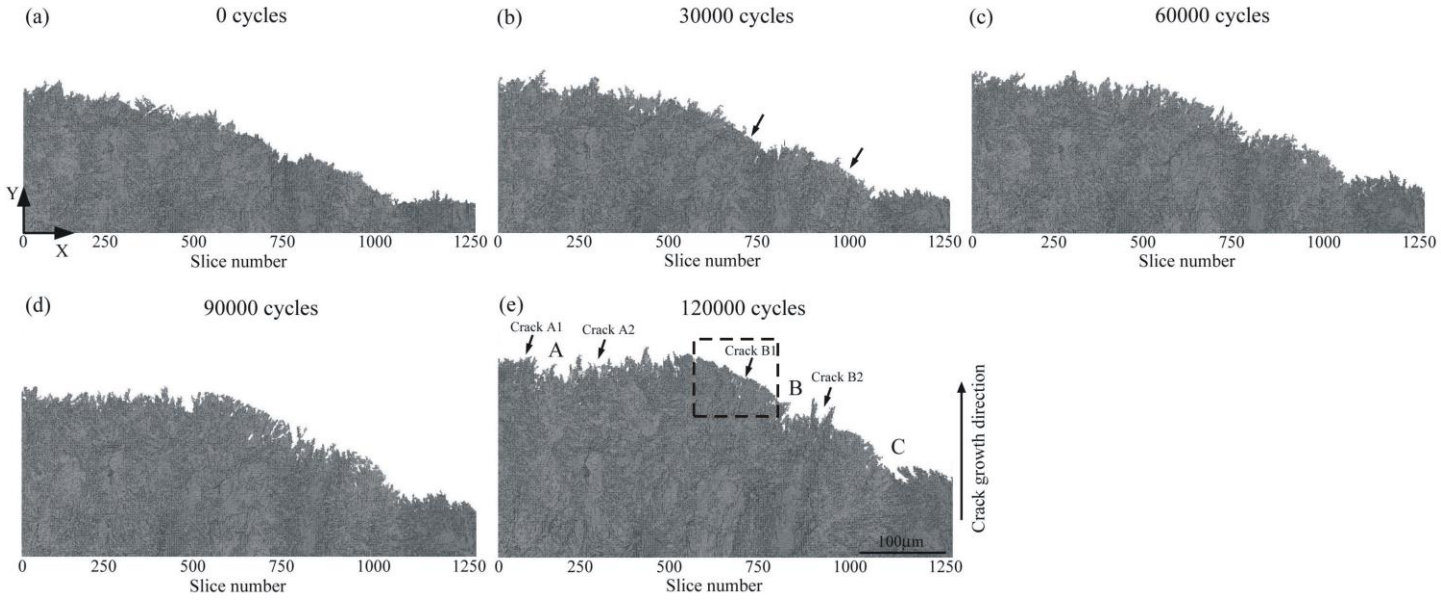
(a)
0 cycles
Y
X
0
250
500
750
1000
1250
Slice number
(b)
30000 cycles
0
250
500
750
1000
1250
Slice number
(c)
60000 cycles
0
250
500
750
1000
1250
Slice number
(d)
90000 cycles
0
250
500
750
1000
1250
Slice number
(e)
120000 cycles
Crack A1
Crack A2
A
Crack B1
B
Crack B2
C
100μm
Crack growth direction
0
250
500
750
1000
1250
Slice number

Figure 2

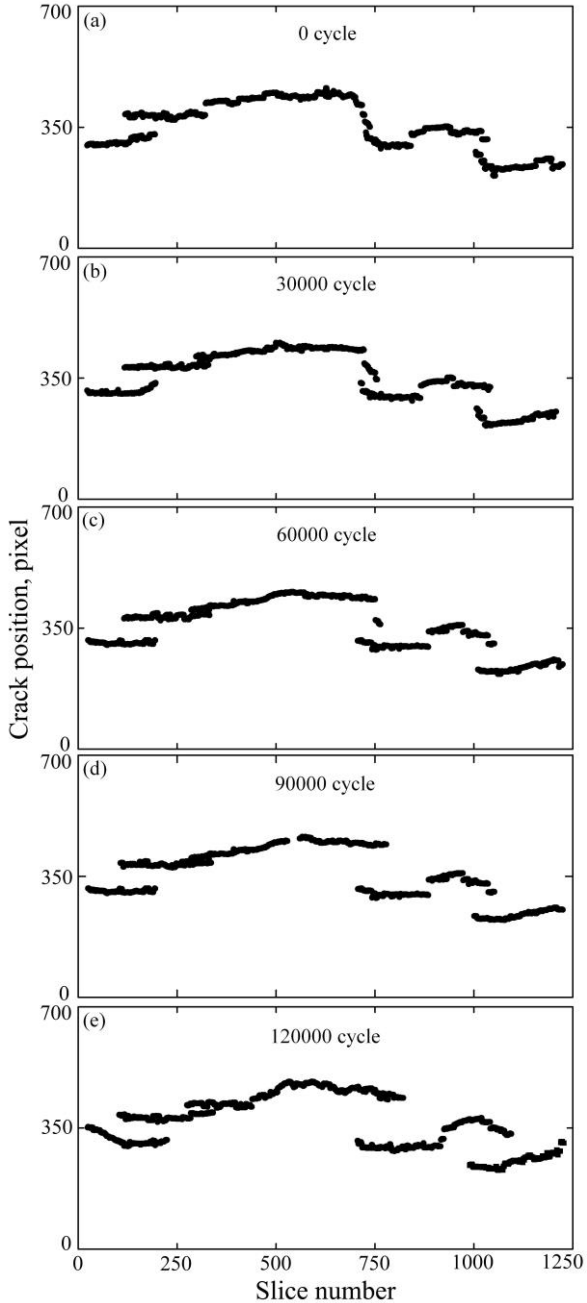
(a)
0 cycle
(b)
30000 cycle
(c)
60000 cycle
(d)
90000 cycle
(e)
120000 cycle
700
350
0
Crack position, pixel
0
250
500
750
1000
1250
Slice number

Figure 3

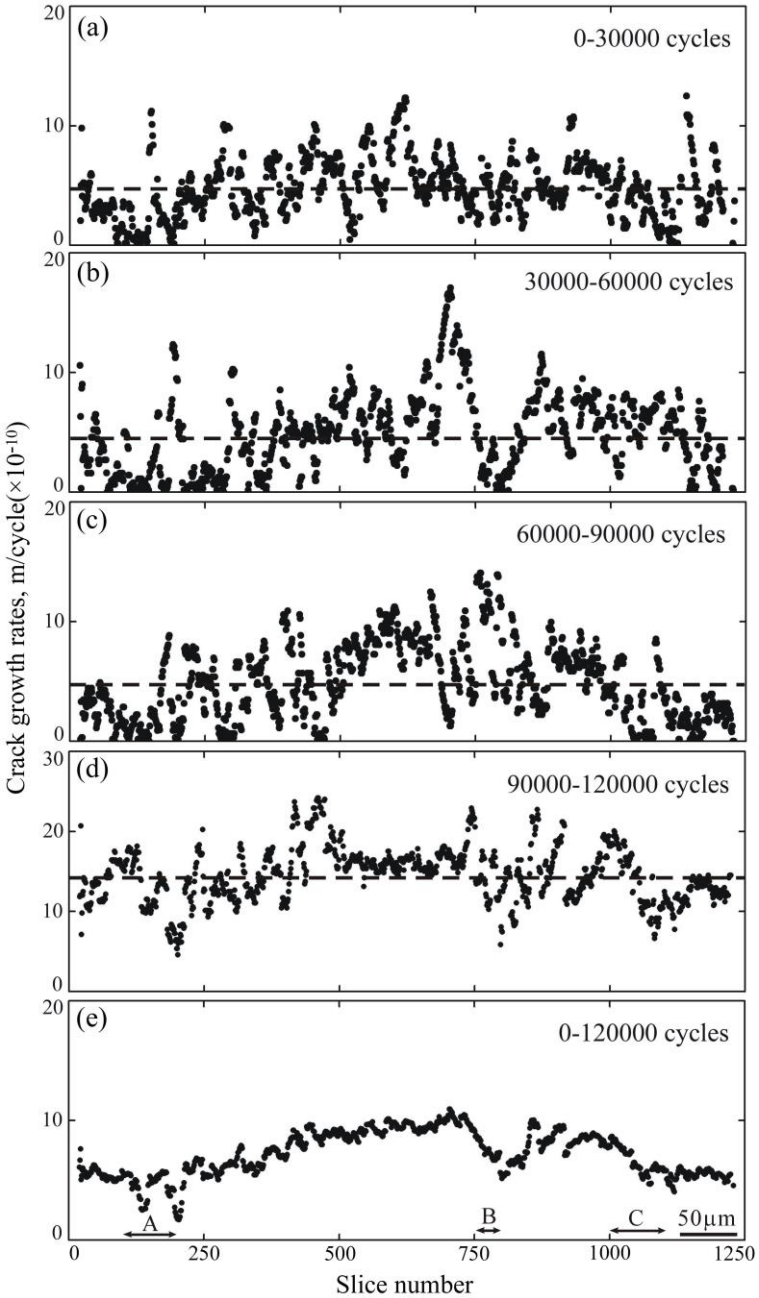
(a)
0-30000 cycles
(b)
30000-60000 cycles
(c)
60000-90000 cycles
(d)
90000-120000 cycles
(e)
0-120000 cycles
A
B
C
50μm
Crack growth rates, m/cycle(×10⁻¹⁰)
Slice number
0
250
500
750
1000
1250

Figure 4

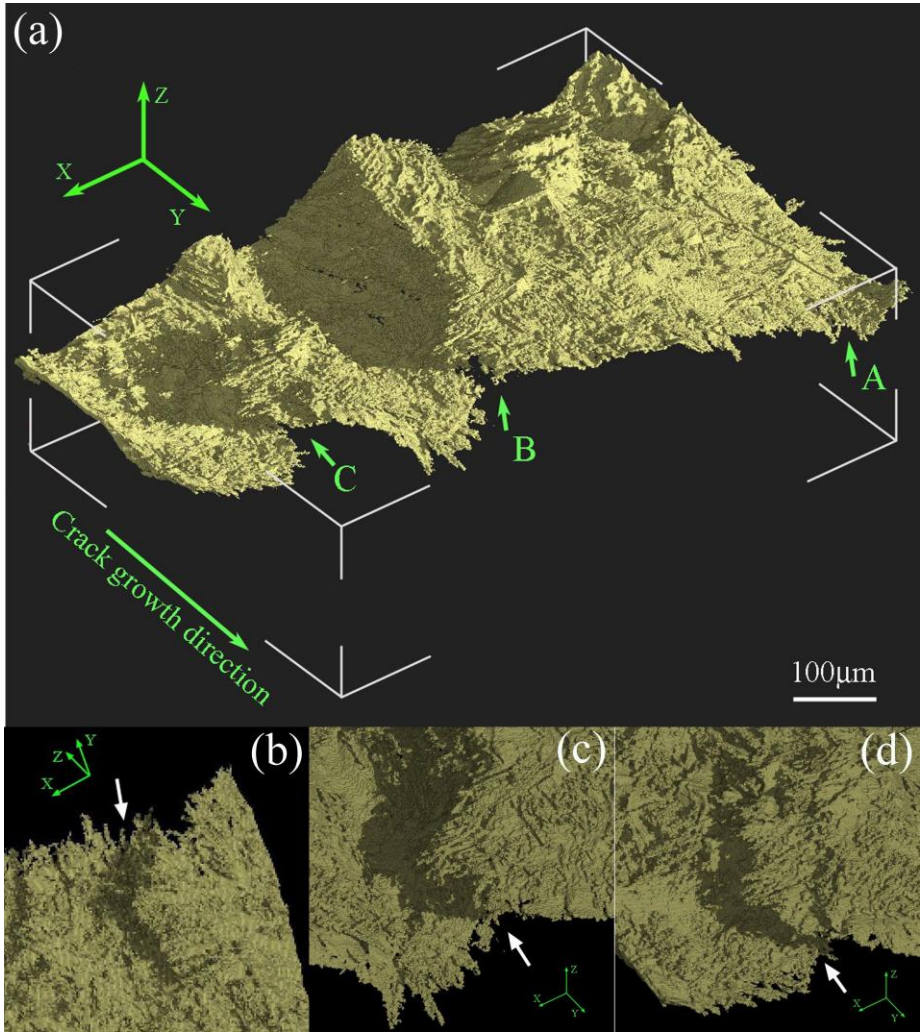

Figure 5

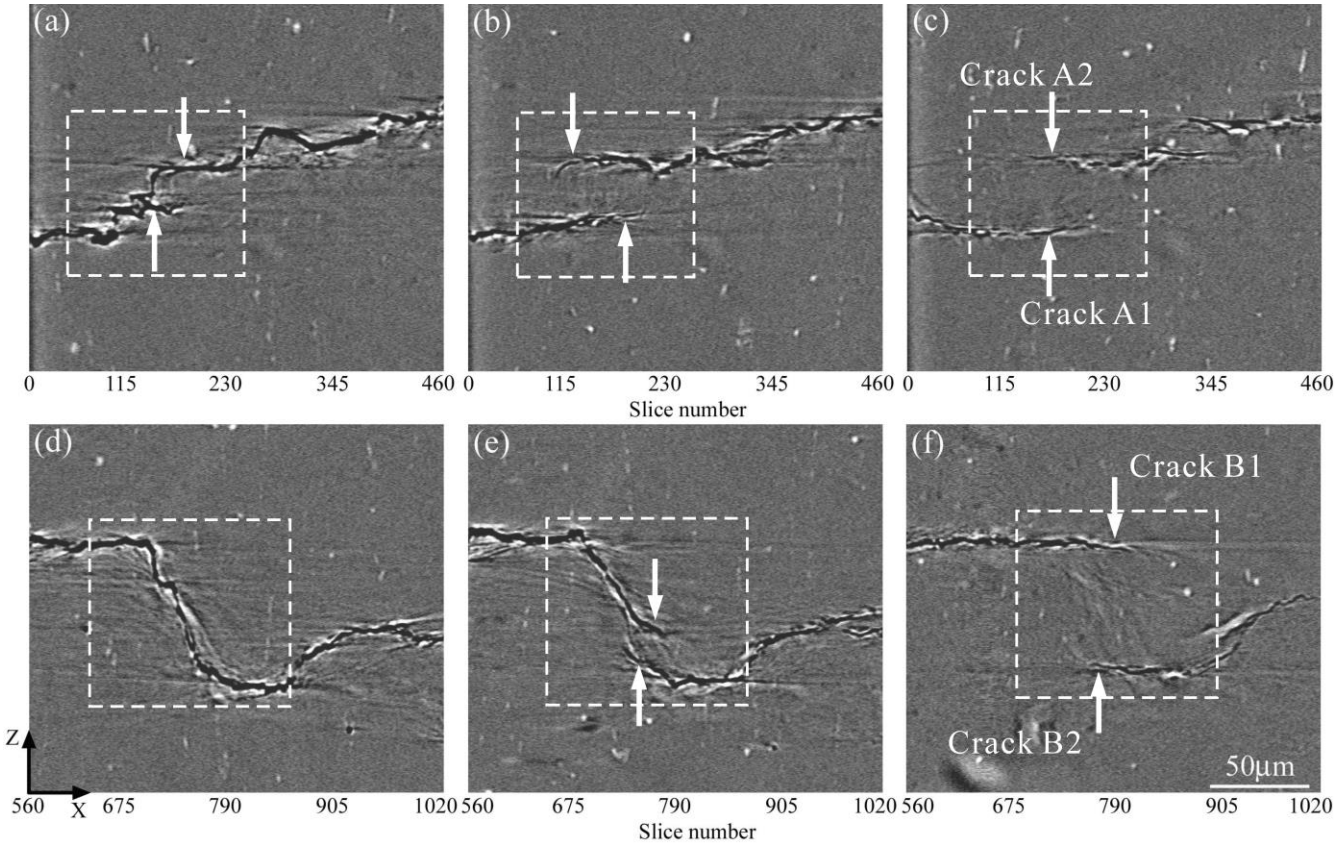
(a)
(b)
(c)
Crack A2
Crack A1
0
115
230
345
460
Slice number
(d)
(e)
(f)
Crack B1
Crack B2
50μm
Z
X
560
675
790
905
1020
Slice number

Figure 6

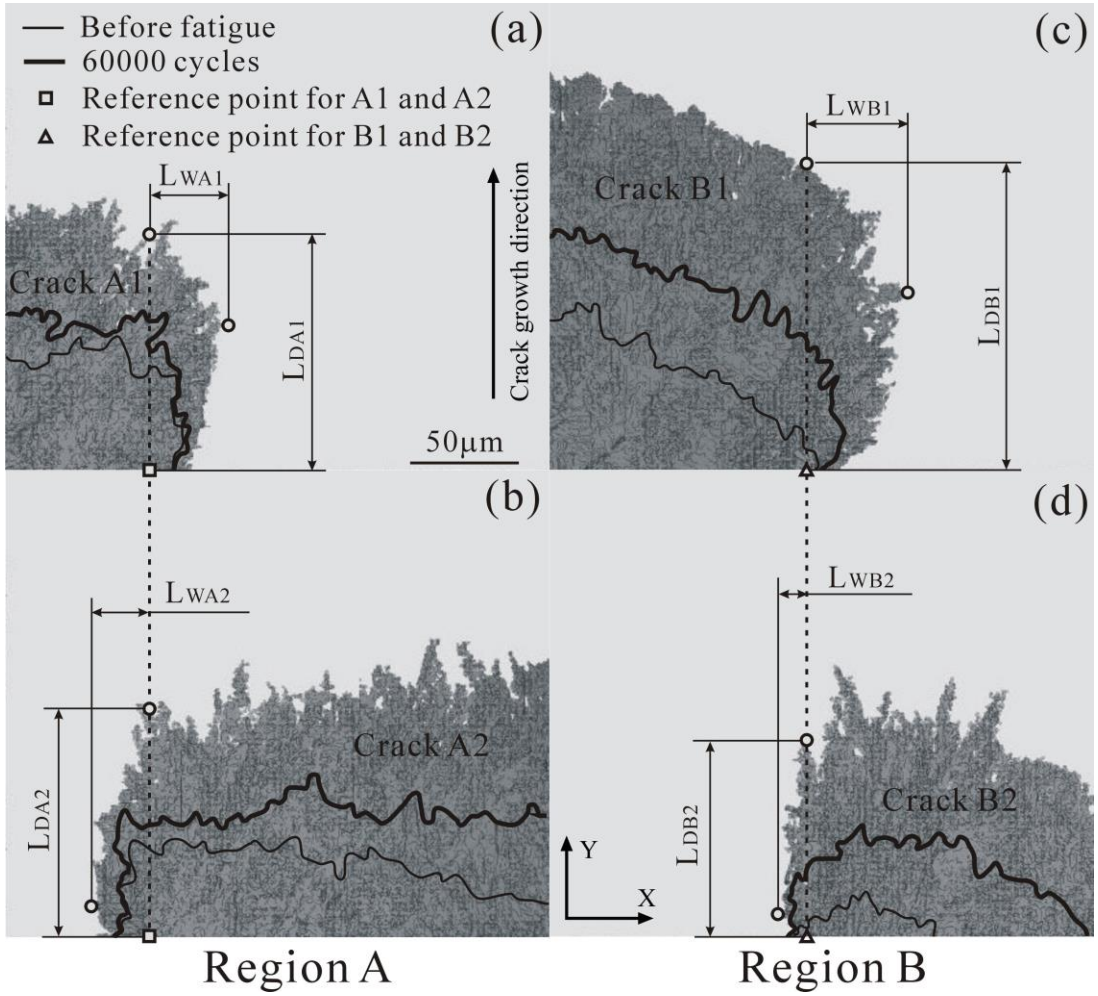
Before fatigue
60000 cycles
Reference point for A1 and A2
Reference point for B1 and B2
(a)
(b)
(c)
(d)
LWA1
LDA1
Crack A1
Crack growth direction
50μm
LWB1
LDB1
Crack B1
LWA2
LDA2
Crack A2
Y
X
LWB2
LDB2
Crack B2
Region A
Region B

Figure 7

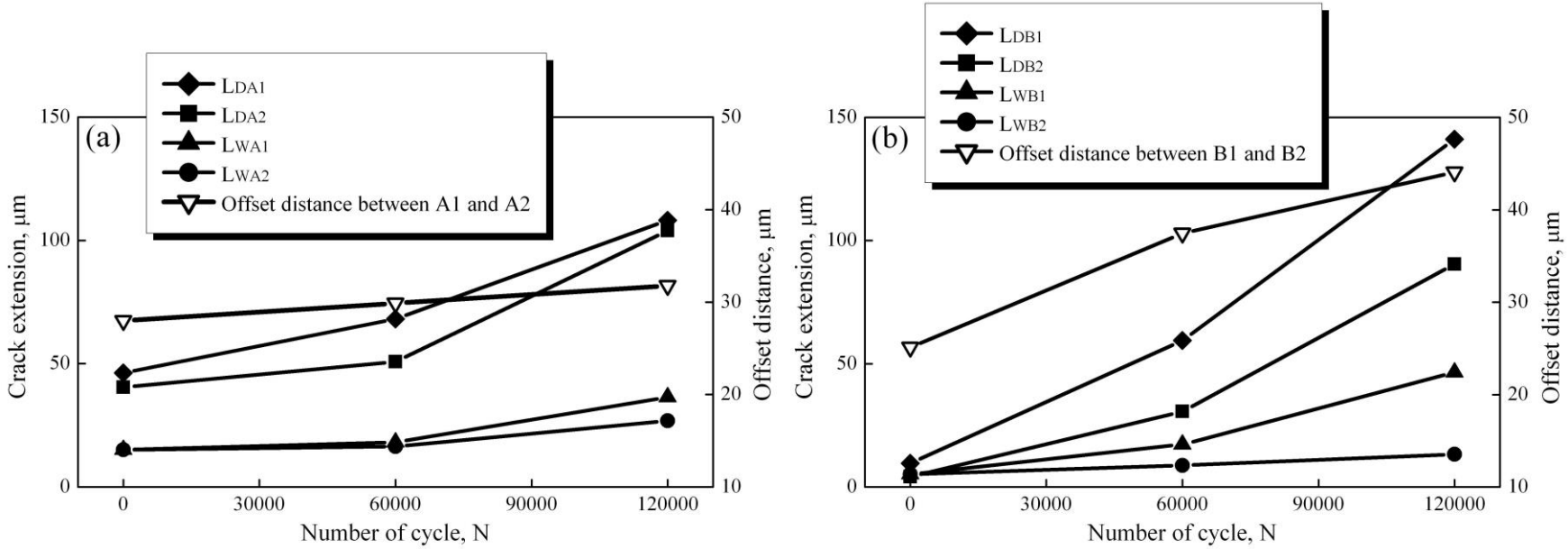
(a)
LDA1
LDA2
LWA1
LWA2
Offset distance between A1 and A2
Crack extension, μm
Offset distance, μm
Number of cycle, N
0
30000
60000
90000
120000
0
50
100
150
10
20
30
40
50
(b)
LDB1
LDB2
LWB1
LWB2
Offset distance between B1 and B2
Crack extension, μm
Offset distance, μm
Number of cycle, N

Figure 8

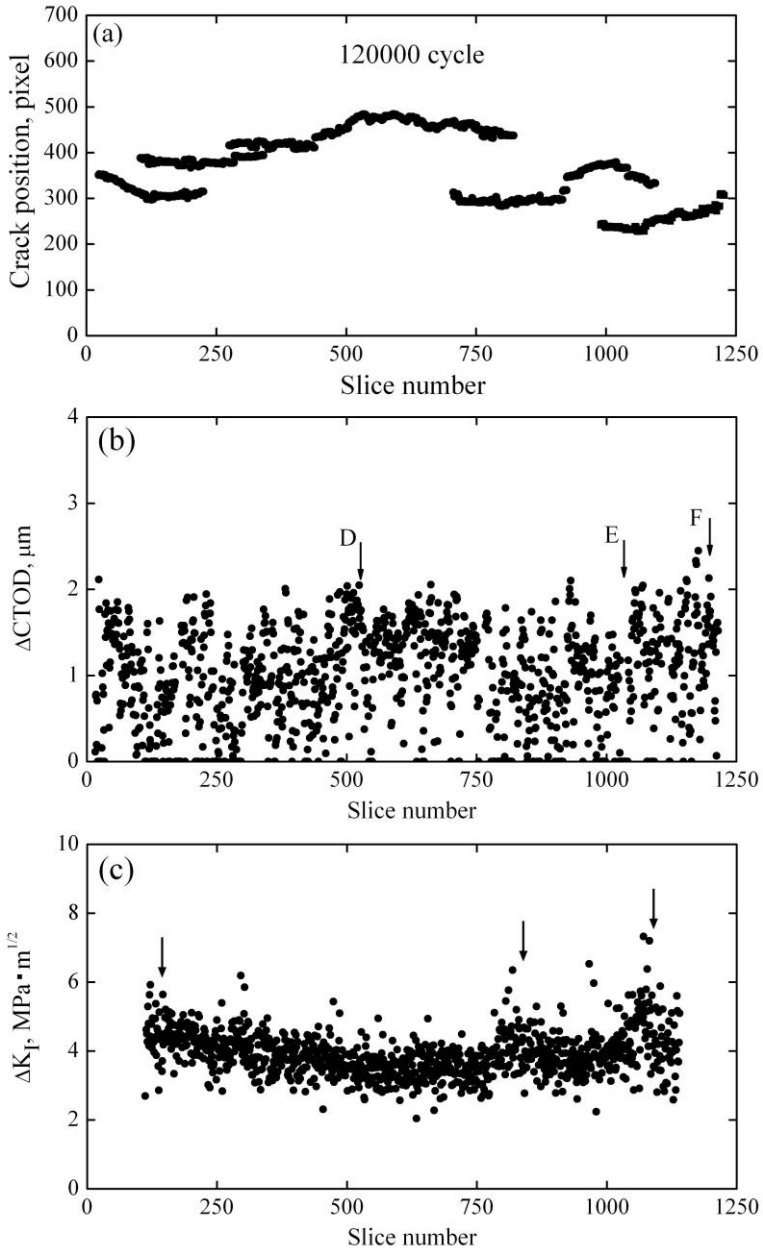
(a)
120000 cycle
Crack position, pixel
Slice number
(b)
D
E
F
ΔCTOD, μm
Slice number
(c)
ΔK_I, MPa · m$^{1/2}$
Slice number

Figure 9

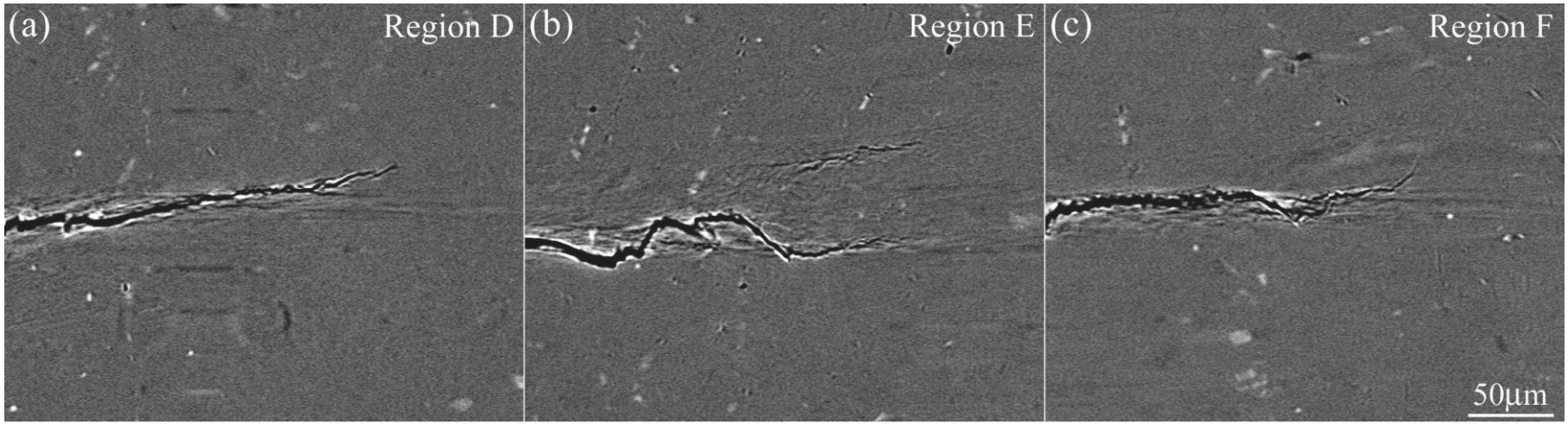

Figure 10

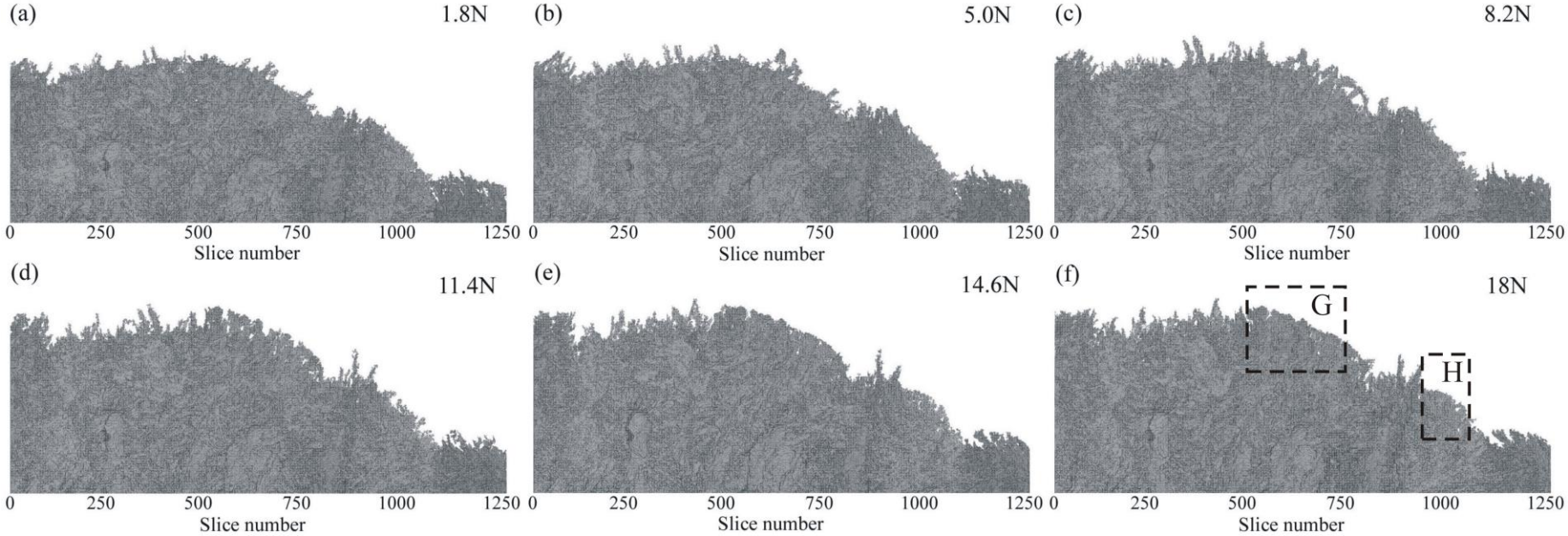
(a)
1.8N
(b)
5.0N
(c)
8.2N
(d)
11.4N
(e)
14.6N
(f)
18N
G
H
0
250
500
750
1000
1250
Slice number

Figure 11

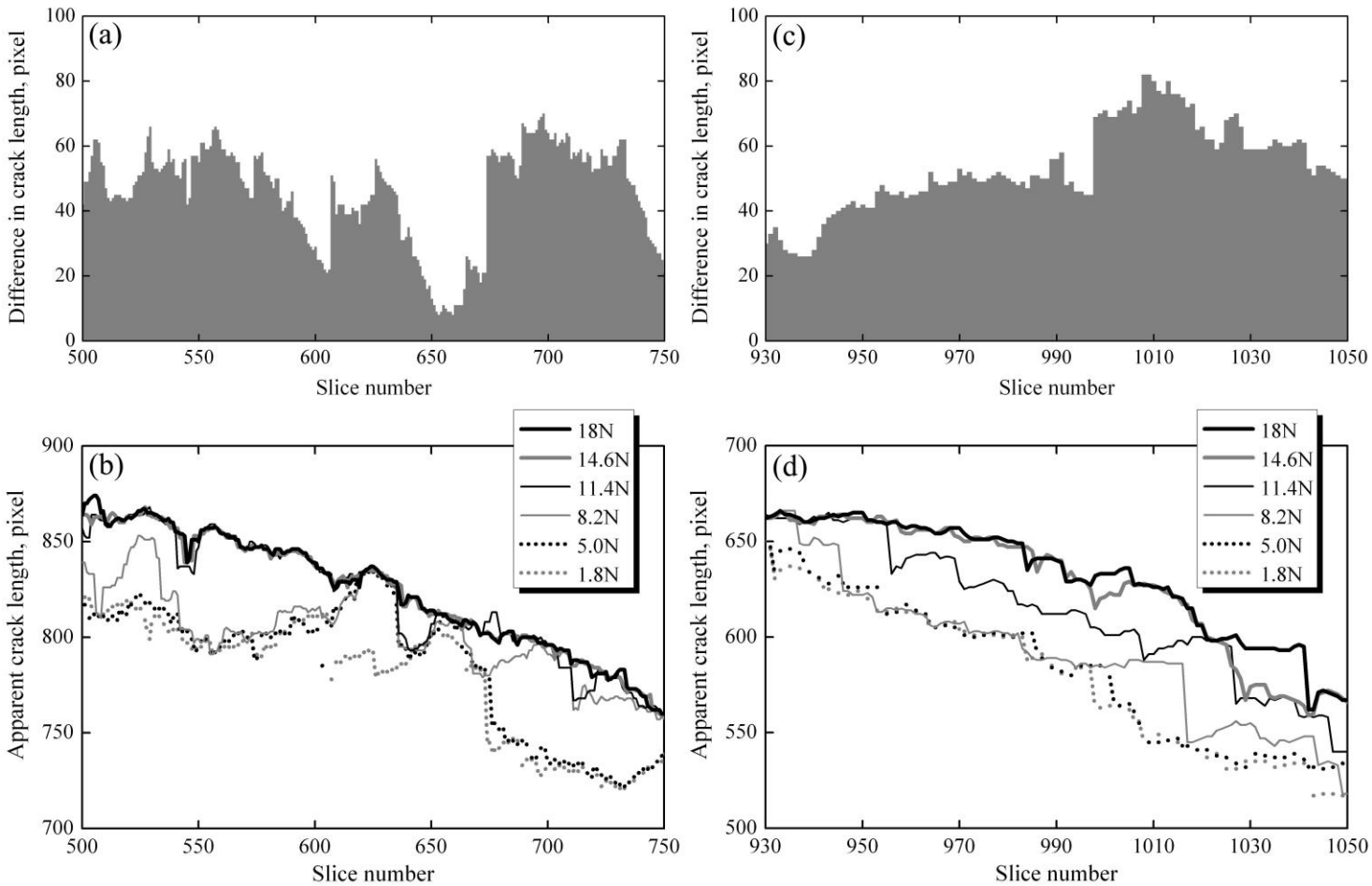
(a)
Difference in crack length, pixel
Slice number
(c)
Difference in crack length, pixel
Slice number
(b)
Apparent crack length, pixel
Slice number
18N
14.6N
11.4N
8.2N
5.0N
1.8N
(d)
Apparent crack length, pixel
Slice number
18N
14.6N
11.4N
8.2N
5.0N
1.8N

Figure 12

Table 1 Chemical composition (mass%) of cast Al-Mg-Si alloy

Mg	Si	Fe	Cu	Mn	Ti	Zn	Cr
0.42	0.35	0.12	<0.01	<0.01	<0.01	<0.01	<0.01